Supplementary information for: Navigating the Land-Energy Nexus for China's Carbon-Neutral Power System

Ziheng Zhu[*#], Runxin Yu[*#], and Da Zhang[*]

[#] These authors contribute equally to this work.
[*]Corresponding author;
E-mail: mrziheng@outlook.com; runxinyu@outlook.com; zhangda@tsinghua.edu.cn.

October 25, 2025

Contents

1 The CISPO Model **1**
1.1 Regions and grids 1

2 Assessment of wind and solar power **2**
2.1 Assessment of the hourly capacity factor for wind power 3
2.2 Assessment of the hourly capacity factor for solar photovoltaic power 7
2.3 Assessment of the hourly capacity factor for concentrating solar power 9
2.4 Assessment of suitable area for developing wind, utility-scale solar photovoltaic power and concentrating solar power 10
2.5 Assessment of suitable area for developing distributed solar photovoltaic power 16
2.6 Assessment of installation capacity potential 20

List of Tables

S1 Province names, abbreviations, and corresponding grid region. 2
S2 Technical parameters of the wind turbine selected by CISPO. 4
S3 Threshold values that are unsuitable for developing wind and utility-scale solar PV power, considering natural conditions. C: Conservative, B: Base, O: Open. 11
S4 Suitability factor of each land use type for determining suitable areas for onshore wind and utility-scale solar. C: Conservative, B: Base, O: Open. 13
S5 Land use classification and definition used in this study. 14
S6 Onshore wind turbine parameters. 21
S7 Offshore wind turbine parameters. 21
S8 Provincial installation capacity potential (GW) of onshore wind in mainland China. 22
S9 Provincial installation capacity potential (GW) of offshore wind in mainland China. 23
S10 Provincial installation capacity potential (GW) of UPV and DPV in mainland China. 25

List of Figures

S1 Framework of the CISPO model. 1
S2 Region division in this model. 2
S3 Assessment process for wind and solar power. 3
S4 Normalized power output curve of different wind power models [1]. 4
S5 Illustration of the fitting results of the normalized power output curve for the selected wind turbine models. 5
S6 Cell level annual average capacity factor (0–1) for onshore and offshore wind power in 2019. 7
S7 Cell level annual average capacity factor (0–1) for solar photovoltaic power in 2019. 8
S8 Simplified schematic of a parabolic trough power plant. Graphic: © NREL/Parthiv and Craig [2] 9
S9 Cell level annual average capacity factor (0–1) for concentrating solar power in 2019. 10
S10 Suitable area (km^2) for wind (a, b, and c) and utility-scale solar PV (d, e, and f) in open, base, and conservative scenarios. 15
S11 Suitable area (km^2) for concentrating solar power in open (a), base (b), and conservative (c) scenarios. 16
S12 Framework for rooftop area assessment using XGBoost regression model. 17
S13 Illustration of Roof Vector Data Area. 17
S14 Correlation coefficient between rooftop area and road length (A), built-up area (B), population (C), and night lights (D). 18
S15 Rooftop area (km^2) of training data (A) fed into XGBoost model, and predicted results (B) by the trained XGBoost model. 19

S16 Suitable area (km^2) for building distributed solar PV in each grid cell in open (a), base (b), and conservative (c) scenario. 20
S17 Installation capacity potential (MW) for onshore and offshore wind power in each grid cell in open (a), base (b) and, conservative (c) scenarios. 22
S18 Installation capacity potential (MW) for utility-scale (a, b, and c) and distributed solar PV (d, e, and f) in each grid cell in open, base, and conservative scenario. 24
S19 Installation capacity potential (MW) for concentrating solar power in each grid cell in open (a), base (b), and conservative (c) scenarios. 26

1 The CISPO Model

The China Integrated Sustainable Power-system Optimization Model (CISPO) is designed to simulate the dynamic changes and hourly operations within China's power systems resulting from novel investments in power generation, storage, and transmission spanning the target period (e.g., from 2030–2060) within a given optimization step (e.g., 10 years). Within each planning year interval, CISPO optimizes the least-cost portfolio, considering input assumptions related to future electric demand, investment costs, technology performance parameters, planning and operating reserves, inertia requirements, and energy availability factors including installation capacity potential and hourly generation profiles. The technologies incorporated into the CISPO model encompass variable renewable energies (VREs), including onshore and offshore wind, utility-scale and distributed solar photovoltaic (PV), concentrating solar power (CSP), hydropower, thermal power (coal, natural gas, and biomass energy), nuclear power, battery storage, pumped hydro storage (PHS), and both intra-grid and inter-grid transmission (alternating current (AC) and direct current (DC)). The data exchange across planning years encompasses the installed and retired capacity of generation. We show the model framework in Figure S1.

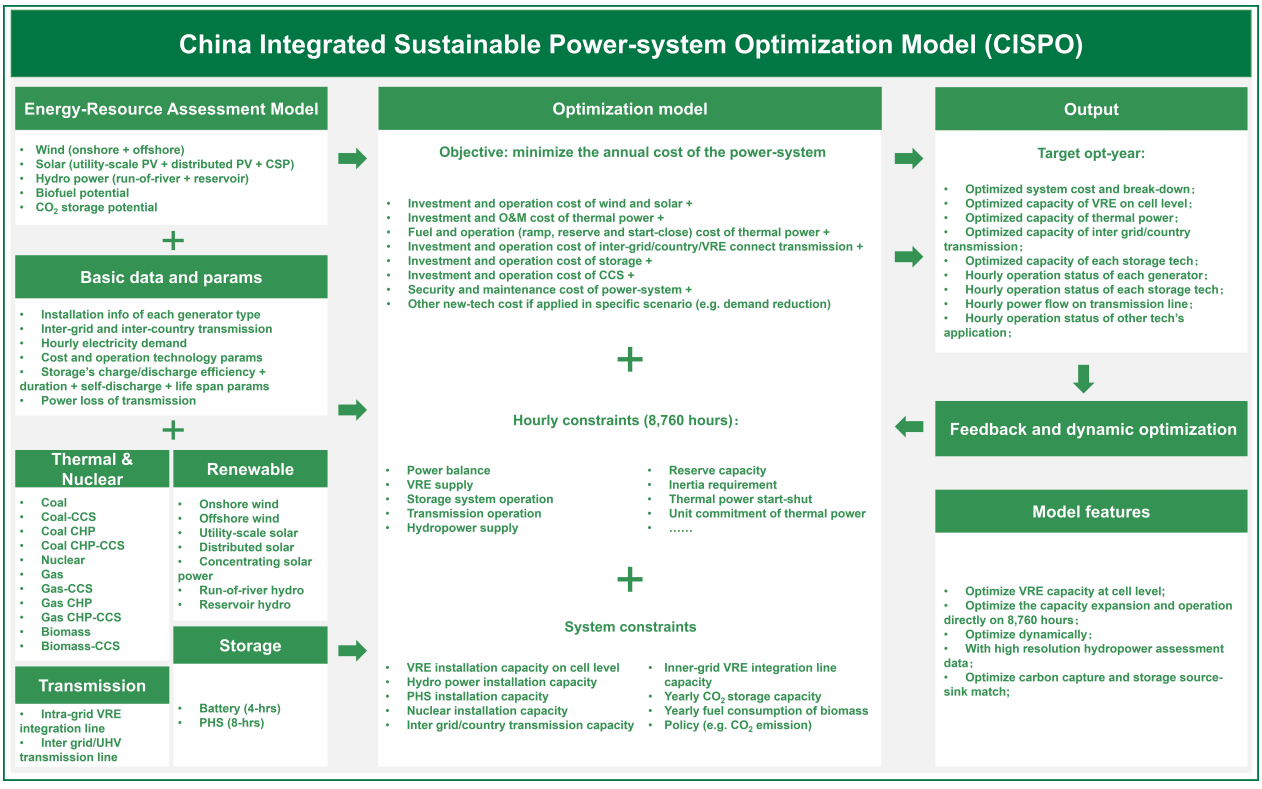

Figure S1: Framework of the CISPO model.

1.1 Regions and grids

In this model, we optimize various parameters at the provincial level, including power balance, electric flow, energy storage deployment, dispatch route, and unit commitment of thermal and nuclear power, while also addressing grid safety requirements (inertia and reserve requirements). The model encompasses a total of

32 provinces, with Inner Mongolia divided into two regions, namely Mengdong and Mengxi, due to their different grid region connections. Throughout the model formulation section, these provinces are denoted as the power grid; refer to Table S1 and Figure S2 for an overview of the regional division and their corresponding designations. VREs are optimized at the cell level (0.25°×0.25°, approximately 25×25 km at middle altitude in this study) for both capacity expansion and power dispatch. Additionally, these for hydropower are considered at the dam site level.

Table S1: Province names, abbreviations, and corresponding grid region.

Province	Abbr.	Grid region	Province	Abbr.	Grid region	Province	Abbr.	Grid region
Anhui	AH	East	Hainan	HI	South	Sichuan	SC	Central
Beijing	BJ	North	Heilongjiang	HL	Northeast	Shandong	SD	North
Chongqing	CQ	Central	Hunan	HN	Central	Shanghai	SH	East
Fujian	FJ	East	Jilin	JL	Northeast	Shaanxi	SN	Northwest
Guangdong	GD	South	Jiangsu	JS	East	Shanxi	SX	North
Gansu	GS	Northwest	Jiangxi	JX	Central	Tianjin	TJ	North
Guangxi	GX	South	Liaoning	LN	Northeast	Xinjiang	XJ	Northwest
Guizhou	GZ	South	Mengdong[a]	MD	Northeast	Xizang	XZ	Xizang
Henan	HA	Central	Mengxi[a]	MX	North	Yunnan	YN	South
Hubei	HB	Central	Ningxia	NX	Northwest	Zhejiang	ZJ	East
Hebei	HE	North	Qinghai	QH	Northwest			

Figure S2: Region division in this model.

2 Assessment of wind and solar power

This section assesses the resource availability of onshore and offshore wind, utility-scale and distributed solar photovoltaic (PV), and concentrating solar power (CSP). The resource assessment of wind and solar power consists of two main components. First is the hourly generation potential, also referred to as the capacity factor (CF$\in$ [0,1]), which represents the ratio between a generator's available output and its nameplate

capacity within a one-hour time frame. Second is the estimate of the maximum installation capacity potential (MW) for each grid cell.

The hourly generation potential of wind and solar power is assessed based on simulation models and meteorological conditions, encompassing wind speed, temperature, surface shortwave solar radiation, and direct short-wave radiation. The maximum installation capacity potential refers to the utmost suitable installation capacity for a given cell, which is determined by installation density (MW/km^2) and suitable development area (km^2). For wind, utility-scale solar PV, and CSP, we estimate the suitable surface land area. For distributed solar PV power, specifically rooftop solar PV in this study, we consider the suitability of the rooftop area. We show the assessment procedure in Figure S3.

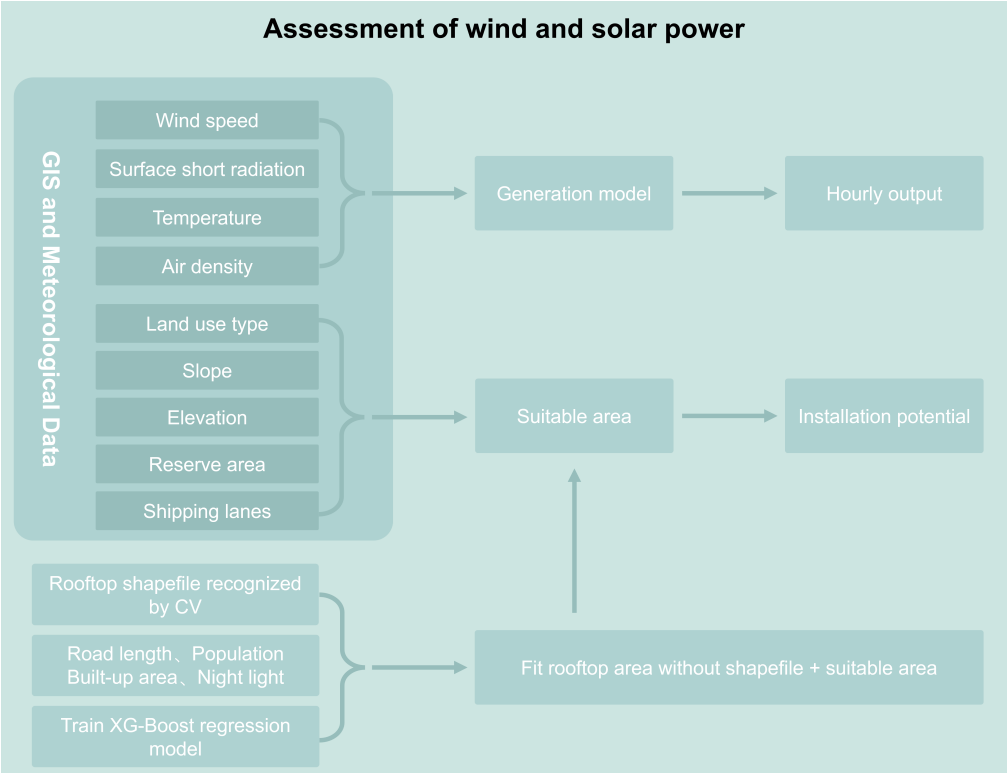

Figure S3: Assessment process for wind and solar power.

2.1 Assessment of the hourly capacity factor for wind power

The hourly capacity factor of wind power is determined by its power output curve and the wind speed at the turbine hub height. The power output curve, along with other technical parameters is the key to assessing the hourly capacity factor for wind power. The National Renewable Energy Laboratory (NREL) provides technical parameters for various wind turbine models in their wind energy assessment project, including nameplate capacity, cut-in, and cut-out wind speeds, rated wind speed, turbine hub height, and power output curve [1]. The hourly capacity factor of onshore and offshore wind power is evaluated using the 2020 ATB NREL Reference 5.5 MW 175 and IEA 15MW 240 RWT turbine models respectively, with the key parameters presented in Table S2. The power output curve of a wind turbine is a piecewise function based on the wind speed (v_w^h, m/s) at the turbine hub height. No power generation occurs when v_w^h is below the

cut-in or above the cut-out wind speed. When the wind speed is between the cut-in and rated wind speeds, the power generation of the turbine exhibits a monotonically increasing behavior to the wind speed. On reaching or exceeding the rated wind speed but remaining below the cut-out wind speed, power generation by the turbine operates at its nameplate capacity. We first normalize the power output curve of wind turbines to assess the hourly capacity factor of wind power. Figure S4 presents normalized power output curves for various turbine types provided by NREL [1]. Considering that the uncertainty lies solely within the segment from cut-in to rated wind speed in the power output curve, we employ a third-degree polynomial fitting method to establish a functional relationship within this range. The results of this fitting process are shown in Figure S5.

Table S2: Technical parameters of the wind turbine selected by CISPO.

	2020ATB NREL Reference 5.5MW 175	IEA 15MW 240 RWT
nameplate capacity (MW)	5.5	15.0
hub height (m)	120.0	150.0
cut-in wind speed (m/s)	3.25	3.00
cut-out wind speed (m/s)	25.0	25.0
rated wind speed (m/s)	10.0	10.6

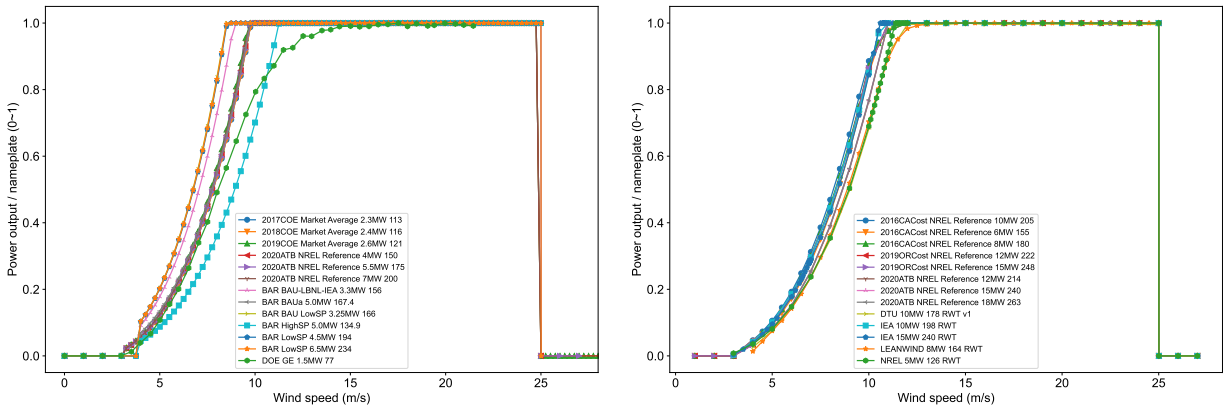

(a) Onshore wind power

(b) Offshore wind power

Figure S4: Normalized power output curve of different wind power models [1].

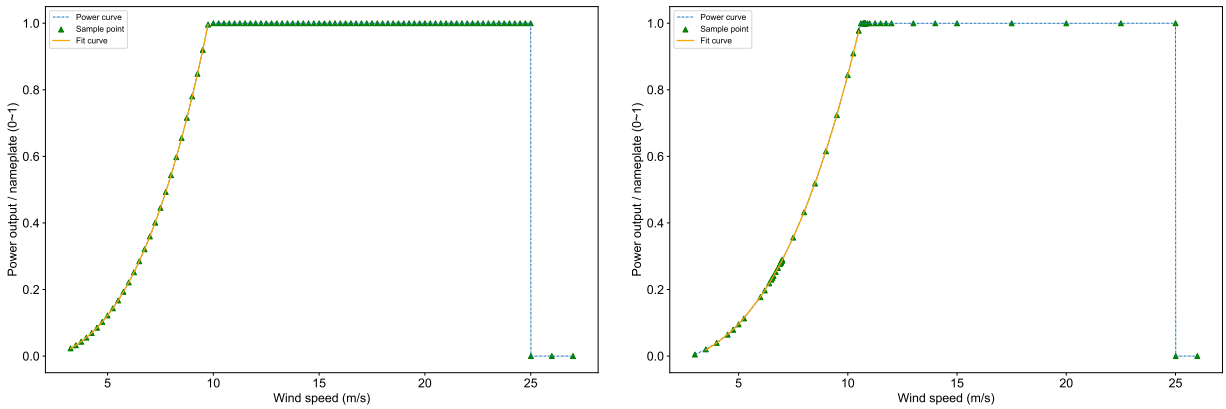

(a) Onshore wind power

(b) Offshore wind power

Figure S5: Illustration of the fitting results of the normalized power output curve for the selected wind turbine models.

Wind speed at the turbine hub height is a critical input for evaluating the capacity factor of wind power. We use the original meteorological data from the European Centre for Medium-Range Weather Forecasts Reanalysis Version 5 (ERA5) dataset, which provides a comprehensive record of global climate and weather spanning over eight decades with a spatial resolution of 0.25° × 0.25° and hourly temporal resolution [3]. The ERA5 dataset includes wind speed data at 10 m and 100 m heights (U10m, V10m, U100m and V100m, m/s). As shown in Table S2, the hub heights of the selected turbine models in this study are 120 m and 150 m for onshore and offshore wind, respectively. Therefore, we use the vertical power law profile to estimate the target height wind speed based on the 10 m and 100 m wind speed data. The wind vertical power law profile is expressed as:

$$v_w^h = v_w^{100} \times (\frac{z_h}{z_{100}})^{\alpha}, \tag{S2-1}$$

where v_w^h is the wind speed at height h (m/s), v_w^{100} is the wind speed at 100 m height (m/s) which is calculated using $v_w^{100} = \sqrt{U_{100}^2 + V_{100}^2}$, z_h is the target height (120 m for onshore wind and 150 m for offshore wind), and $z_{100} = 100$ m, α is wind shear coefficient which is a parameter varying as a function of the terrain where wind farms are located. We apply equation S2-1 based on the wind speeds at 10 m and 100 m to estimate the value of α for each hour at each 0.25° × 0.25° grid cell.

The power output curve of a wind turbine is standardized based on measurements made under conditions of standard air density (ρ_{std}^h=1.225 kg/m^3). Therefore, when calculating power output at a given moment using the power output curve, it is necessary to convert the observed wind speed to the equivalent wind speed under standard air density. The relationship between wind speed under standard conditions (v_{std}^h) and measured conditions (v_{meas}^h) is described by the following equation [4]:

$$v_{std}^h = v_{meas}^h \times \left(\frac{\rho_{meas}^h}{\rho_{std}^h}\right)^{1/3}, \tag{S2-2}$$

in this equation, v_{std}^h is the wind speed at height h under standard air density, v_{meas}^h is the measured wind speed calculated using Equation S2-1, and ρ_{meas}^h is the actual air density. However, ERA5 reanalysis data

does not directly provide observed air density. Instead, air density must be calculated based on other reported meteorological variables using the ideal gas state equation [4]:

$$\rho^h_{meas} = \frac{p^h_{meas} - p_{vapour}}{R_{dry}T} + \frac{p_{vapour}}{R_{vapour}T}, \tag{S2-3}$$

where R_{dry} is the gas constant for dry air (287.1 J/kg·K), R_{vapour} is the specific gas constant for water vapor (461.5 J/kg·K), p^h_{meas} is the measured atmospheric pressure (Pa) at hub height (h), p_{vapour} is the partial pressure (Pa) of water vapor at 2 m height, and T is the temperature at hub height (K). The partial pressure of water vapor (p_{vapour}) can be determined from the relative humidity of the air (%, ϕ) and the temperature using the Clausius-Clapeyron equation:

$$p_{vapour} = \phi \times 610.78 \times \exp\left(\frac{17.27(t - 273.15)}{t - 273.15 + 237.3}\right), \tag{S2-4}$$

where t is the temperature at 2 m height. We assume that the partial pressure of water vapor at hub height is equal to that at 2 m [4]. And the air humidity (ϕ) can be calculated according to the dewpoint temperature (K) at 2 m height from the ERA5 data using the equation [5]:

$$\phi = \exp\left(\frac{17.625 \times (t_d - 273.15)}{243.04 + (t_d - 273.15)} - \frac{17.625 \times (t - 273.15)}{243.04 + (t - 273.15)}\right) \times 100\%. \tag{S2-5}$$

Finally, we calculate the atmospheric pressure (Pa) at hub height (h), denoted as p^h_{meas}, using the surface pressure from ERA5 (Surface pressure, Pa, p_0), by:

$$p^h_{meas} = p_0 \times e^{-\frac{gh}{R_d t}}, \tag{S2-6}$$

where e is the base of the natural logarithm, g = 9.81 m/s^2 is the gravitational acceleration at the earth's surface, t is the temperature at 2 m height, and R_d is a function of the specific humidity of the air (q, kg/m^3):

$$R_d = qR_{vapour} + \frac{R_{dry}}{1 + q}. \tag{S2-7}$$

After wind speed at the hub height under standard air density is obtained through the previously described calculations, the hourly capacity factor for wind power generation can be determined for each $0.25° \times 0.25°$ cell using the normalized power output curve of the wind turbine model. Additional adjustments to the capacity factor are then made based on the following considerations:

- The capacity factor at each timestep is decreased by 5% due to factors such as wake effects and electrical losses in wind farms [6, 7].
- The wind turbine ceases operation when the temperature at the hub height drops below -30°C due to extreme cold, leading to a correction of the capacity factor to 0 [4].
- The wind turbine ceases operation when the wind speed surpasses the cut-out threshold and can only be reactivated upon meeting specific wind speed criteria. CISPO employs a hysteresis window approach to address this concern, whereby the wind turbine can only resume operation once the wind speed falls below or equals 20 m/s for the first time after shutdown. The cut-out threshold of the wind turbine can be found in Table S2.

In the CISPO model, the geographical scope considered for offshore wind power is limited to China's Exclusive Economic Zone (EEZ) [8]. In Figure S6, we show the annual average capacity factor ($\sum_{t \in T} cf_t/|T|$) for both onshore and offshore wind power at each grid cell in 2019.

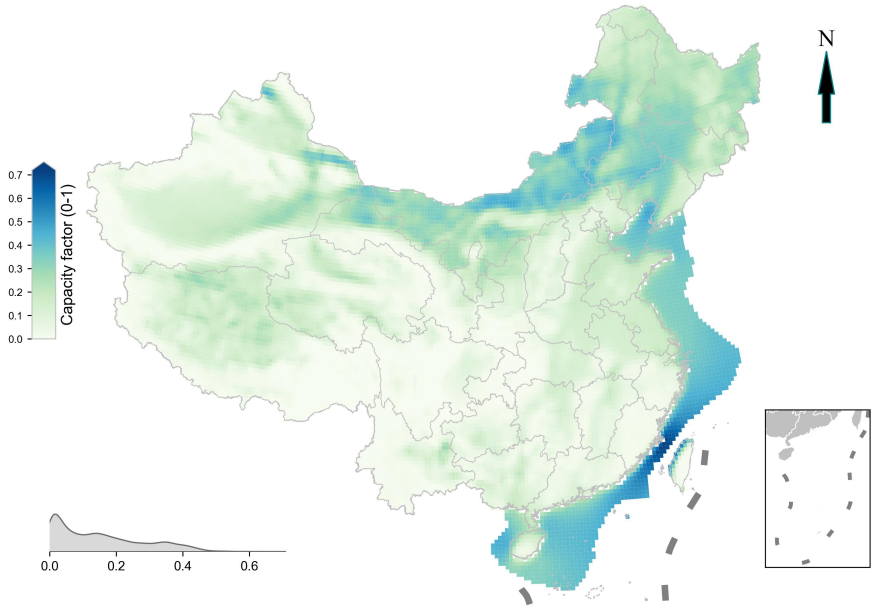

Figure S6: Cell level annual average capacity factor (0–1) for onshore and offshore wind power in 2019.

2.2 Assessment of the hourly capacity factor for solar photovoltaic power

To quantify the hourly capacity factor of solar PV power at a given grid cell, we implement the fixed tilt photovoltaic system model [9]. The solar PV power output constitutes a fraction of the nameplate capacity, which can be derived from meteorological data. Specifically, we use the ERA5 hourly meteorological dataset [3], which provides measurements of surface downwelling shortwave radiation (SSRD2M, J/m^2), surface temperature (T2m, K), and 10-meter height surface wind speed (U10m and V10m, m/s) at a 0.25°×0.25° spatial resolution. Based on these inputs, we assess the DC power output to the nameplate capacity fraction using the following equation [10]:

$$\frac{P_{dc}}{P_{dc0}} = [1 + \gamma \times (T_{cell}(t) - T_{std})] \times \frac{ssrd(t)}{ssrd_{std}} \times \eta_{sys}, \tag{S2-8}$$

where P_{dc}/P_{dc0} is the fraction of the DC output to the nameplate capacity, $T_{cell}(t)$ is the temperature of the solar PV module's cell, T_{std} is the PV panel's cell temperature under standard test conditions (25 °C), γ is the temperature coefficient of the solar PV cell, which is set as -0.005 °C^{-1} reflecting the efficiency at different temperatures, $ssrd(t)$ is the hourly surface downwelling shortwave radiation (W/m^2, converting from J/m^2) in the environment, which can be derived from SSRD2M variable in the ERA5 data, $ssrd_{std}$ is the shortwave flux on the solar PV panel under standard test conditions, defined as 1,000 W/m^2, and $\eta_{sys} \in [0, 1]$ is the efficiency of the DC electric system, set as 0.86 [10, 11].

According to previous studies, the ambient temperature ($T_{cell}(t)$, °C) of solar PV cell can be calculated using the following equation based on surface downwelling shortwave radiation ($ssrd(t)$, W/m^2), ambient

temperature ($T(t)$, °C), and wind speed ($v_w(t)$, m/s) [12, 13]:

$$T_{cell}(t) = c_1 + c_2 \times T(t) + c_3 \times ssrd(t) + c_4 \times v_w(t), \tag{S2-9}$$

where c_1 =4.3 °C, c_2 =0.943, c_3 =0.028 °C·m^2·W^{-1}, $c_4 = -1.528$ °C·s·m^{-1}, $T(t)$ is the hourly ambient temperature, and $v_w(t)$ is the hourly surface wind speed. And then the rearrangement of equations S2-8 and S2-9 yields:

$$\frac{P_{dc}}{P_{dc0}} = [\alpha_1 \times ssrd(t) + \alpha_2 \times ssrd(t)^2 + \alpha_3 \times ssrd(t) \times T(t) + \alpha_4 \times ssrd(t) \times v_w] \times \eta_{sys}, \tag{S2-10}$$

where $\alpha_1 = 1.1035 \times 10^{-3}$, $\alpha_2 = -1.4 \times 10^{-7}$, $\alpha_3 = -4.715 \times 10^{-6}$, $\alpha_4 = 7.64 \times 10^{-6}$, and the calculated P_{dc}/P_{dc}^0 is a dimensionless quantity. The AC output of the PV module can be derived according to PVWatts [11] by:

$$\frac{P_{ac}}{P_{ac0}} = \min(\eta \times \frac{P_{dc}}{P_{ac0}}, 1), \tag{S2-11}$$

where P_{ac}/P_{ac0} is the fraction of the AC output to the nameplate capacity, $P_{ac0} = \eta_{nom} \times P_{dc0}$ is the nameplate AC capacity, and $\eta_{nom} = 0.96$ is the nominal DC-AC inverter efficiency, and the η is a function of P_{dc}/P_{dc0} with the inverting performance given by [11] as:

$$\eta = \frac{\eta_{nom}}{\eta_{ref}} \times (-0.0162 \times \zeta - \frac{0.0059}{\zeta} + 0.9858), \tag{S2-12}$$

where $\zeta = P_{dc}/P_{dc0}$, and $\eta_{ref} = 0.9637$ is reference inverter efficiency. Combining formula S2-10, S2-11, and S2-12, the fraction of the AC output to the nameplate capacity is:

$$\frac{P_{ac}}{P_{ac0}} = \min\left(\frac{1}{\eta_{ref}} \times (-0.0162 \times \zeta^2 + 0.9858 \times \zeta - 0.0059), 1\right). \tag{S2-13}$$

We consider that utility-scale and distributed solar PV within the same cell share the same capacity factor value. We show the annual average capacity factor for solar PV in 2019 in each grid cell in Figure S7.

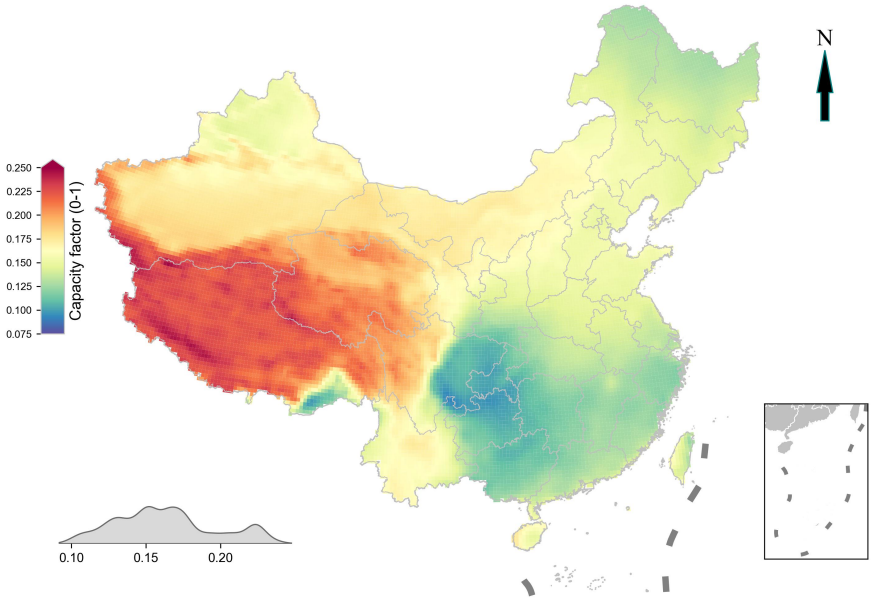

Figure S7: Cell level annual average capacity factor (0–1) for solar photovoltaic power in 2019.

2.3 Assessment of the hourly capacity factor for concentrating solar power

Concentrating solar power (CSP) technologies leverage the heat of the sun to power a thermoelectric generation cycle. In this study, the parabolic trough collector (PTC) is used as the representative CSP technology to assess the available resources. Trough-power plants employ extensive arrays of solar collectors featuring a reflective parabolic surface to concentrate sunlight onto a receiver pipe (Figure S8). A heat transfer fluid (HTF), commonly a synthetic oil, circulates through the receiver and is heated by the absorbed solar irradiation. This heated fluid is then used to generate high-pressure steam, which drives a conventional steam turbine generator to produce electricity. The steam exiting the turbine is condensed back into water and recirculated by feedwater pumps to be converted into high-pressure steam once more.

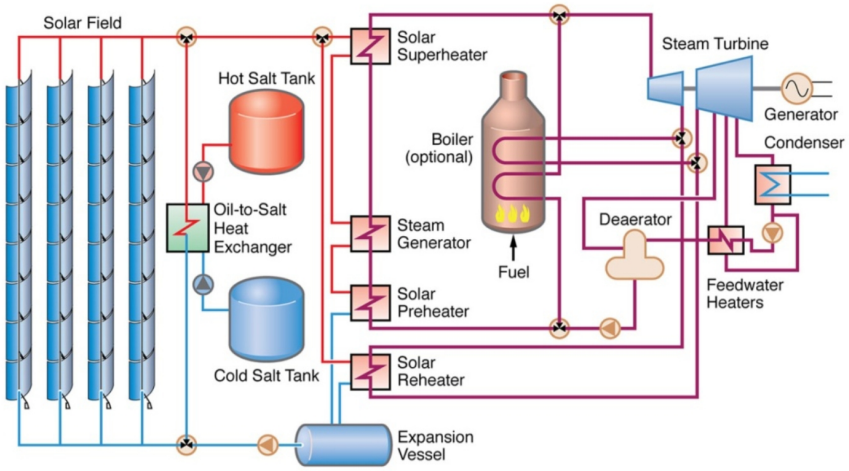

Figure S8: Simplified schematic of a parabolic trough power plant. Graphic: © NREL/Parthiv and Craig [2]

Different from solar PV power systems, concentrating solar power technologies harness the direct normal irradiance (DNI) and use the captured thermal energy by transferring it to a heat transfer fluid. To evaluate the energy generation potential of CSP systems, we employ the surface direct shortwave radiation (dsr) data from the ERA5 reanalysis dataset. The generation potential per unit area (W/m^2) at timestep t, denoted as P_t, is given by the following expression [14, 15]:

$$P_t = \eta_R \times (k_0 \times dsr_t - k_1 \times (T_f - T_{ai})) \tag{S2-14}$$

where η_R represents the Rankine cycle efficiency (assumed to be 40%), k_0 is 0.762, dsr_t is the direct shortwave radiation (W/m^2), k_1 is 0.2125 W/(m^2°C^1), T_f is the temperature of the fluid in the absorber, and T_{ai} is the ambient temperature. The quantity P_t assessed here corresponds to the technical generation potential using a PTC system. Based on the installed projects and the projected technology improvements, we set the maximum generation capacity of the per-area PTC collector at 100 W/m^2, denoted as P_i, and estimate the capacity factor as:

$$cf_t = \min(\frac{P_t}{P_i}, 1). \tag{S2-15}$$

This equation constrains the maximum generation of the PTC system to the installed nameplate capacity. We show the annual average capacity factor of the PTC system at the cell level in Figure S9.

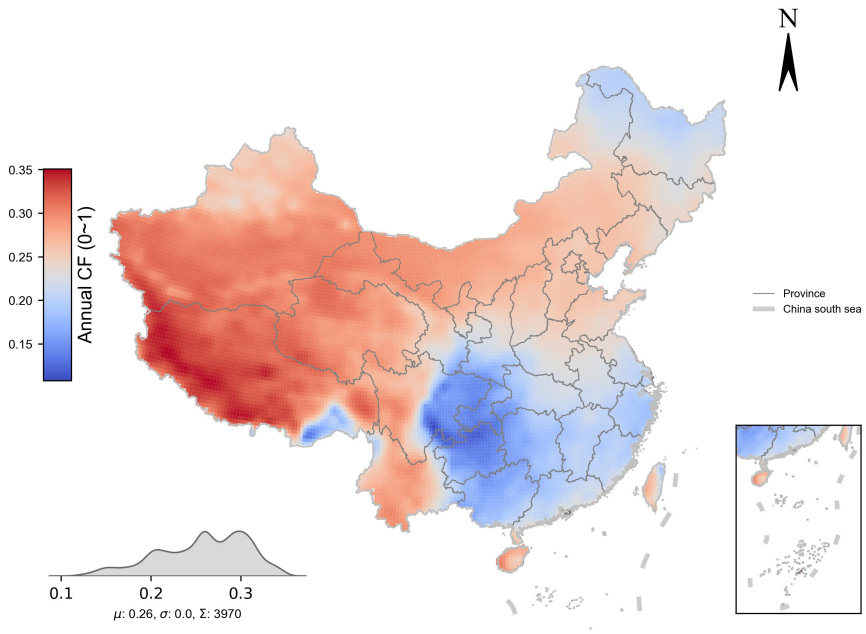

Figure S9: Cell level annual average capacity factor (0–1) for concentrating solar power in 2019.

2.4 Assessment of suitable area for developing wind, utility-scale solar photovoltaic power and concentrating solar power

We estimate the installation capacity potential of wind and solar power based on the suitable land area and assumed installation density [16, 17] for each 0.25° × 0.25° grid cell, consistent with the resolution of the ERA5 meteorological data. To evaluate the suitable land area for developing wind and solar PV power, we employ the China Land Use/Cover Change Dataset (CNLUCC) for 2020 [18], provided by the Resource and Environmental Science and Data Center of the Chinese Academy of Sciences (RESDC), which is represented at the "pixel" level within each grid cell. The CNLUCC land use dataset adopts a two-level classification system. Level 1 categorizes land into six primary types: cropland, forest land, grassland, inland water areas, urban and built-up land, and unused land. Level 2 further delineates these into 24 specific land use types. Definitions for each land use type are provided in Table S5. We initially exclude the pixels within each grid cell that are situated in nature reserves and biodiversity reserve areas due to environmental protection reasons [19, 20]. Subsequently, we formulate three scenarios (open, base, and conservative) to further eliminate the remaining pixels that do not meet natural condition constraints such as steep slopes, high altitudes, and water depths. Additionally, for offshore wind applications, pixels located within shipping lanes are also omitted for safety considerations. Following these steps, the suitability factor is devised for the three scenarios to estimate the suitable area within the remaining pixels based on land use types to represent different policy requirements. Finally, we aggregate the suitable area of qualified pixels in each grid cell to

determine the total suitable area for developing wind, utility-scale solar PV power, and concentrating solar power.

The threshold values[1] for the natural conditions are presented in Table S3. For the shipping lanes in these three scenarios, offshore pixels with shipping density larger than the threshold are excluded. We use the shipping density data from World Bank [24], which is derived from IMF's analysis of hourly AIS positions received between Jan-2015 and Feb-2021, representing the total number of AIS positions reported by ships in each grid cell at $0.005° \times 0.005°$ resolution (approximately a 500 m $\times$ 500 m grid cell at the Equator) [24]. Following the recommendations from the previous study [25], we adopt the historical 90th, 85th, and 80th percentile shipping density to identify the shipping lanes for open, base, and conservative scenarios, respectively, to filter out the unsuitable pixels. The corresponding absolute values for these percentiles are about 400, 235, and 104 ships per hour.

Table S3: Threshold values that are unsuitable for developing wind and utility-scale solar PV power, considering natural conditions. C: Conservative, B: Base, O: Open.

Natural condition	Onshore wind			Offshore wind			Utility-scale solar			CSP		
	C	B	O	C	B	O	C	B	O	C	B	O
Slope (%)	>15	>20	>25	-	-	-	>3	>5	>7	>3	>5	>7
Altitude (m)	>3000	-	-	-	-	-	-	-	-	-	-	-
Water depth (m)	-	-	-	>40	>60	>100	-	-	-	-	-	-

After excluding pixels that are located in nature reserves or biodiversity conservation regions, and do not satisfy natural condition constraints or safety requirements for shipping, we estimate the suitable area of the remaining pixels by designing the suitability factor, which is defined as the ratio of the suitable area for deployment to the total area of a pixel, for each land use type according to policies and previous studies [16, 17, 26–28]. Finally, we determine the suitable land area for each grid cell by aggregating suitable areas of all the pixels within it.

The Chinese government has advocated for the widespread adoption of renewable energy sources, including wind, solar PV, and CSP, particularly on underutilized land parcels designated as level 1 ID 6 (unused land) in the CNLUCC dataset. In 2019, the Ministry of Natural Resources issued a mandate emphasizing the imperative utilization of unused land for infrastructural development [29]. This directive was further reinforced in 2023, when the Ministry reaffirmed its endorsement of repurposing both unused land and extant construction plots for the advancement of photovoltaic power generation [30]. Because of the land-intensive nature of utility-scale solar PV and CSP installations, as compared to the smaller footprints of wind turbines, lower suitability factors are assigned to utility-scale solar PV and CSP (40%) projects than onshore wind (80%) installations in the unused land type. Since the lands used in the installed CSP projects are primarily desert and state-owned unused lands [31], the authors have selected only the unused land (level 1 ID 6) for

[1]Data source: The slope data is from OpenTopography [21], altitude data is from MERIT [22], and water depth data is from GEBCO [23].

developing CSP. Additionally, we have constrained the sum of the suitability factors for solar PV and CSP in the same land use type to be less than 100%.

The Chinese government has implemented strict regulations to protect permanent basic farmland in order to ensure food security. Article 35 of China's Land Administration Law stipulates that no organization or individual may occupy or change the use of permanent basic farmland without authorization [32]. Similarly, the 2019 Guidelines for Implementing Industrial Land Policies issued by the Ministry of Natural Resources prohibit the construction of land on cropland and mandate the strict protection of permanent basic farmland [29]. This directive was further reinforced in the 2023 Notice on Supporting the Development of Photovoltaic Power Generation Industry, which explicitly states that permanent basic farmland shall not be occupied for any purpose [30]. Due to the lack of public information regarding the detailed boundaries of permanent basic farmland, assumptions must be made based on the CNLUCC data. We consider paddy/irrigated cropland, which includes land equipped with reliable water sources and irrigation facilities, to be consistent with the second category of permanent basic farmland. Accordingly, the suitability factors for wind and solar development on paddy/irrigated cropland are set to 0%. For dry cropland, however, current policies do not strictly prohibit wind or solar PV development if the land is not classified as permanent basic farmland. A conservative assumption is made, setting the suitability factor for solar at 5% in the base case, as solar PV panels require a significant land area. In contrast, wind turbines occupy a much smaller footprint (approximately 0.1% of the total wind farm area), and their impact on farming is limited, leading to a base case suitability factor of 80% for onshore wind development on dry cropland.

We set corresponding suitability factors based on canopy closure of forested areas and percent cover of grasslands, respectively [28]. In 2015, the State Forestry Administration issued a notice prohibiting wind or solar PV development in nature reserves, forest parks (including national parks), habitats of endangered species, natural forest protection project areas, and state-owned forests in Northeast China and Inner Mongolia [19]. In 2019, the State Forestry and Grassland Administration further stipulated strict protection for ecologically important and fragile forest areas, leading to the exclusion of "closed forest land" (level 2 ID 21 in CNLUCC data) from consideration [20]. Additionally, the Grassland Law of the People's Republic of China (Article 38) states that mining and engineering construction should avoid or minimize the occupation of grasslands, resulting in the exclusion of "high coverage grassland" and "moderate coverage grassland" (level 2 ID 31 and 32 in CNLUCC data) [33]. For the remaining forest land and grassland types, the suitability factor is set at 80% for onshore wind and 5% and 20% for utility-scale solar PV, respectively.

The suitability factor for inland water bodies is set at 0% for the reason that the Guiding Opinions on Strengthening the Spatial Regulation and Control of River and Lake Shorelines issued by the Ministry of Water Resources in 2022 stipulate that solar PV power stations, wind power projects, and other constructions shall not be built within river channels, lakes or reservoirs [34].

In urban and built-up areas, the suitability factors for onshore wind were set to 0% considering noise and greater visual impact concerns. For solar PV, a more conservative assumption was made, setting the

suitability factor at 5% in the base case, as solar PV can potentially be deployed on some industrial, mining, and transportation land types.

The detailed suitability factor values for each land use type in three scenarios are listed in Table S4. And the resulting suitable area for developing wind, utility-scale solar power, and concentrating solar power in each grid cell is shown in Figure S10.

Table S4: Suitability factor of each land use type for determining suitable areas for onshore wind and utility-scale solar. C: Conservative, B: Base, O: Open.

Level 1		Level 2		Onshore wind (%)			Utility-scale solar (%)			CSP (%)		
				C	B	O	C	B	O	C	B	O
ID	Name	ID	Name	-	-	-	-	-	-	-	-	-
1	Cropland	-	-	-	-	-	-	-	-	-	-	-
-	-	11	Paddy/irrigated cropland	0	0	0	0	0	0	0	0	0
-	-	12	Dry cropland	60	80	100	0	5	10	0	0	0
2	Forest land	-	-	-	-	-	-	-	-	-	-	-
-	-	21	Closed forest land	0	0	0	0	0	0	0	0	0
-	-	22	Shrubland	60	80	100	0	5	10	0	0	0
-	-	23	Open forest land	60	80	100	0	5	10	0	0	0
-	-	24	Other forest land	60	80	100	0	5	10	0	0	0
3	Grassland	-	-	-	-	-	-	-	-	-	-	-
-	-	31	High coverage grassland	0	0	0	0	0	0	0	0	0
-	-	32	Moderate coverage grassland	0	0	0	0	0	0	0	0	0
-	-	33	Low coverage grassland	60	80	100	15	20	25	0	0	0
4	Inland water area	-	-	-	-	-	-	-	-	-	-	-
-	-	41	Rivers and streams	0	0	0	0	0	0	0	0	0
-	-	42	Lakes	0	0	0	0	0	0	0	0	0
-	-	43	Reservoirs and ponds	0	0	0	0	0	0	0	0	0
-	-	44	Permanent ice and snow	0	0	0	0	0	0	0	0	0
-	-	45	Tidal flats	0	0	0	0	0	0	0	0	0
-	-	46	River/lake shoals	0	0	0	0	0	0	0	0	0
5	Urban and built-up land	-	-	-	-	-	-	-	-	-	-	-
-	-	51	Urban land	0	0	0	0	5	10	0	0	0
-	-	52	Rural settlements	0	0	0	0	5	10	0	0	0
-	-	53	Other construction land	0	0	0	0	5	10	0	0	0
6	Unused land	-	-	-	-	-	-	-	-	-	-	-
-	-	61	Sandy land	80	90	100	30	40	50	30	40	50
-	-	62	Gobi land	80	90	100	30	40	50	30	40	50
-	-	63	Saline-alkali land	80	90	100	30	40	50	30	40	50
-	-	64	Wetland	80	90	100	30	40	50	30	40	50
-	-	65	Bare land	80	90	100	30	40	50	30	40	50
-	-	66	Bare rock	80	90	100	30	40	50	30	40	50
-	-	67	Other unused land	80	90	100	30	40	50	30	40	50

Table S5: Land use classification and definition used in this study.

Level 1		Level 2		Definition
ID	Name	ID	Name	
1	Cropland	-	-	Land used for cultivation of crops, including mature cropland, newly reclaimed land, fallow land, rotation land, grassland used for crop rotation; land used mainly for fruits, sericulture, agroforestry; land reclaimed from shoals and mudflats for over three years.
	-	11	Paddy/irrigated cropland	Land with assured water source and irrigation facilities that can be normally irrigated in a typical year for cultivation of aquatic crops like rice, lotus, etc., including land where rice and upland crops are rotated.
	-	12	Dry cropland	Land without irrigation water source and facilities, relying on natural precipitation for cultivation of crops; land with water source and irrigation facilities that can be normally irrigated for cultivation of upland crops in a typical year; land used mainly for vegetable cultivation; land with normal crop rotation like fallow and rotation land.
2	Forest land	-	-	Land used for forestry purposes with the dominance of trees, shrubs, bamboo, and mangroves along the coastline.
	-	21	Closed forest land	Natural and artificial forests with crown density >30%, including timber forests, economic forests, protected forests, and other large patches of forests.
	-	22	Shrubland	Dwarf forests and shrub forests with crown density >40% and height <2 m.
	-	23	Open forest land	Forest land with crown density of 10-30%.
	-	24	Other forest land	Afforested land but not yet forested, sparse land, nurseries and various orchards (fruit, mulberry, tea, agroforestry orchards, etc.).
3	Grassland	-	-	Various grasslands dominated by herbaceous plants, with vegetation cover >5%, including shrub grasslands used mainly for grazing and open forest grasslands with crown density <10%.
	-	31	High coverage grassland	Natural, improved and mown grasslands with vegetation cover >50%. Such grasslands generally have good moisture conditions and lush grass growth.
	-	32	Moderate coverage grassland	Natural and improved grasslands with vegetation cover 20-50%. Such grasslands generally have insufficient moisture and sparse grass growth.
	-	33	Low coverage grassland	Natural grasslands with vegetation cover 5-20%. Such grasslands lack moisture, have sparse grass growth, and poor grazing conditions.
4	Inland water area	-	-	Natural inland water bodies and water conservancy facilities.
	-	41	Rivers and streams	Naturally formed or artificially dredged rivers and streams, as well as land below the normal water level within river banks, including artificial canals and embankments.
	-	42	Lakes	Naturally formed water bodies and land below the normal water level within lake basins.
	-	43	Reservoirs and ponds	Artificially built water bodies and land below the normal water level within reservoirs and ponds.
	-	44	Permanent ice and snow	Land permanently covered by glaciers and snow.
	-	45	Tidal flats	The intertidal zone between high tide and low tide lines along the coast.
	-	46	River/lake shoals	Land between the normal water level and flood water level of rivers and lakes.
5	Urban and built-up land	-	-	Urban settlements and other built-up land outside settlements like industrial, mining, and transportation facilities.
	-	51	Urban land	Built-up areas of large, medium, and small cities as well as county towns.
	-	52	Rural settlements	Rural settlements independent of urban areas.
	-	53	Other construction land	Land for factories, mines, large industrial zones, oil fields, salt fields, quarries, etc., as well as transportation, airports, and other special purposes.
6	Unused land	-	-	Currently unused land, including land difficult to use.
	-	61	Sandy land	Land covered by sand, with vegetation cover <5%, including deserts but excluding river/lake shoals.
	-	62	Gobi land	Land covered mainly by gravels and rocks, with vegetation cover <5%.
	-	63	Saline-alkali land	Land with salt accumulation on the surface and sparse vegetation that can only grow highly salt-alkali resistant plants.
	-	64	Wetland	Flat and low-lying land with poor drainage, long-term dampness, seasonal or permanent waterlogging, and hydrophytes on the surface.
	-	65	Bare land	Land with soil cover and vegetation cover <5%.
	-	66	Bare rock	Land with >5% cover of rocks or rock fragments on the surface.
	-	67	Other unused land	Other unused land like alpine deserts, tundra, etc.

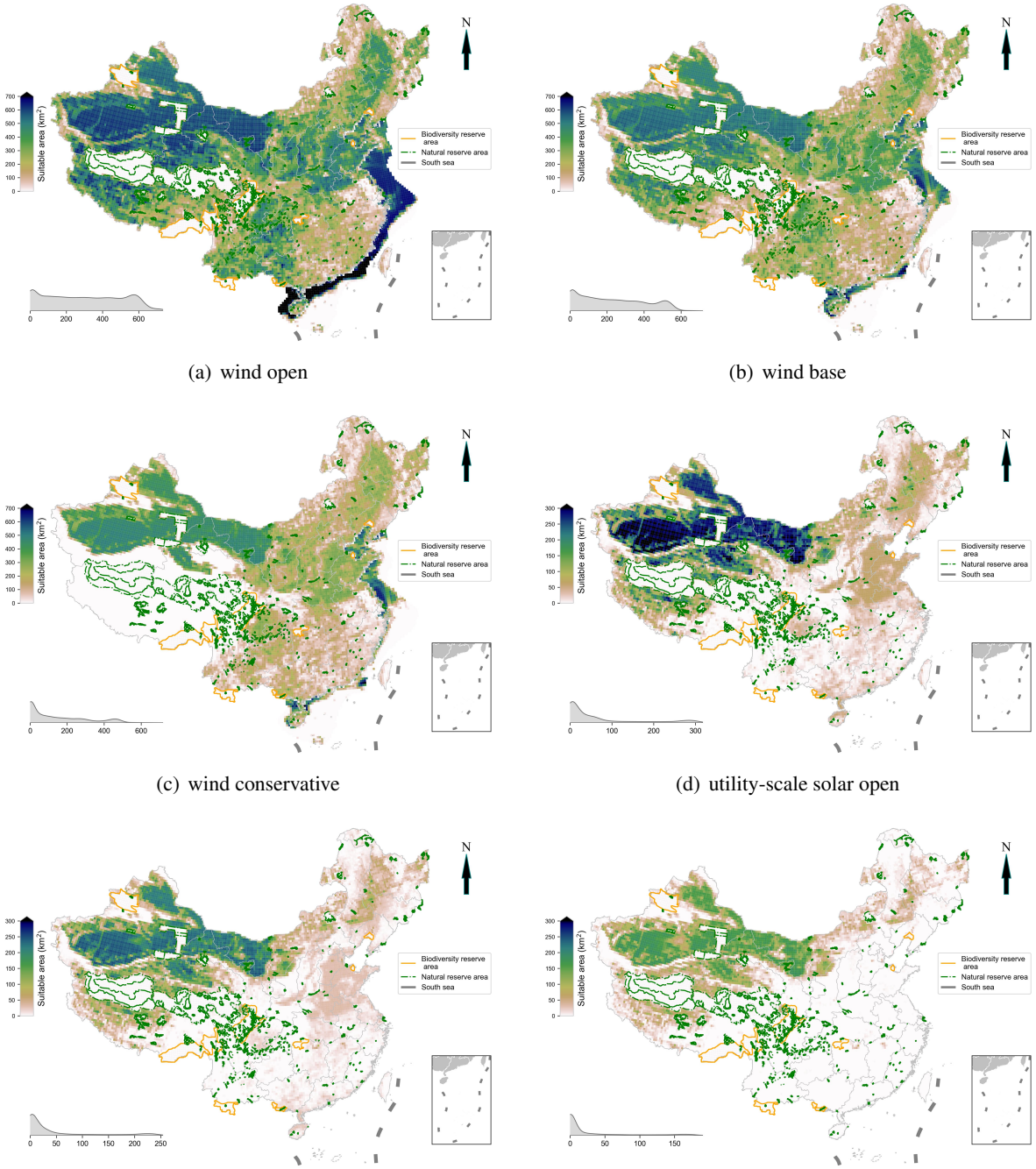

(a) wind open

(b) wind base

(c) wind conservative

(d) utility-scale solar open

(e) utility-scale solar base

(f) utility-scale solar conservative

Figure S10: Suitable area (km^2) for wind (a, b, and c) and utility-scale solar PV (d, e, and f) in open, base, and conservative scenarios.

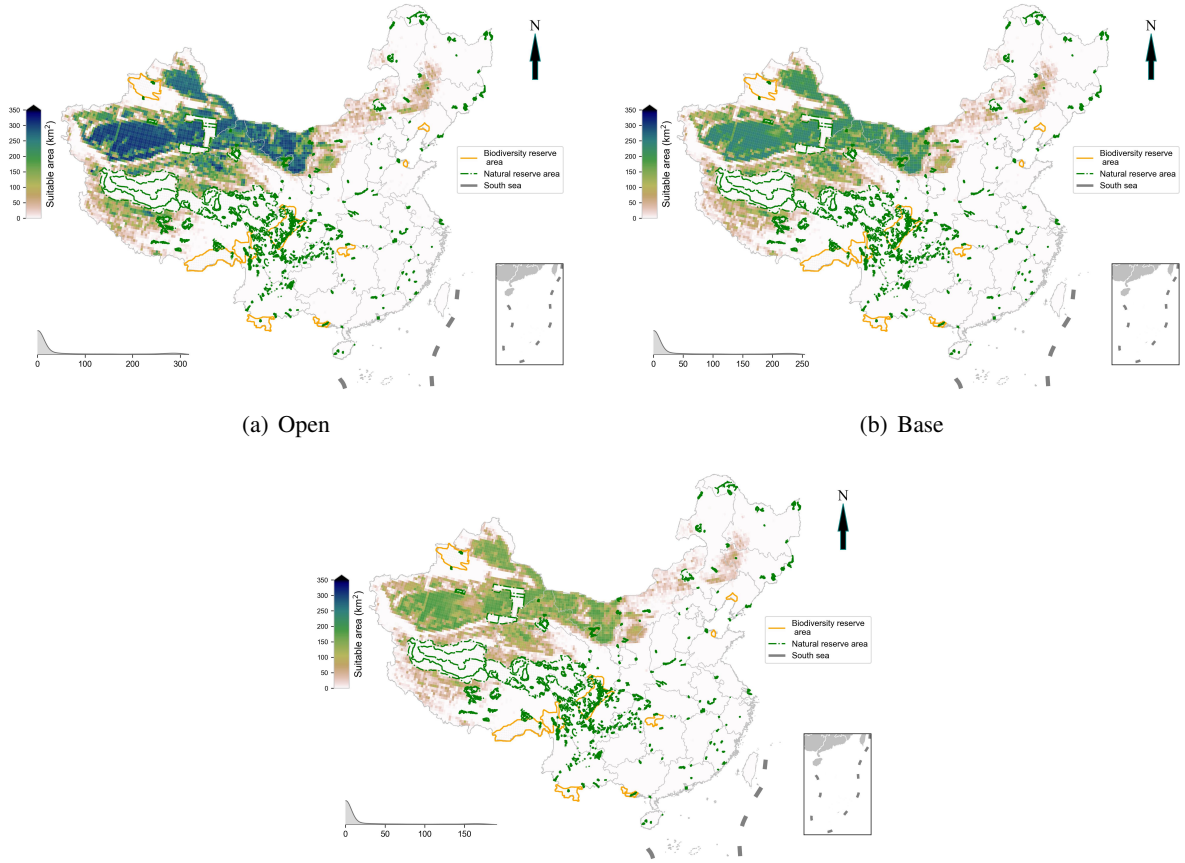

(a) Open

(b) Base

(c) Conservative

Figure S11: Suitable area (km^2) for concentrating solar power in open (a), base (b), and conservative (c) scenarios.

2.5 Assessment of suitable area for developing distributed solar photovoltaic power

Distributed solar photovoltaic (DPV) systems in this study also refer to building-integrated photovoltaic (BIPV). Different from assessments of suitable land areas for wind and utility-scale solar PV power, estimating the suitable area for DPV requires first approximating the total rooftop area available in each grid cell. While previous work has shown that rooftop areas can be accurately determined by integrating remote sensing imagery with deep learning computer vision algorithms [35], obtaining precise rooftop area estimates within an acceptable timeframe remains challenging. To address this, prior studies [36, 37] have demonstrated the feasibility of using an XGBoost regression model to predict rooftop area based on built-up area, population, road length, and night lights in each grid cell. The predictions from this modeling framework, as illustrated in Figure S12, have shown acceptable errors compared to the rooftop areas recognized using the CV algorithm [36, 37].

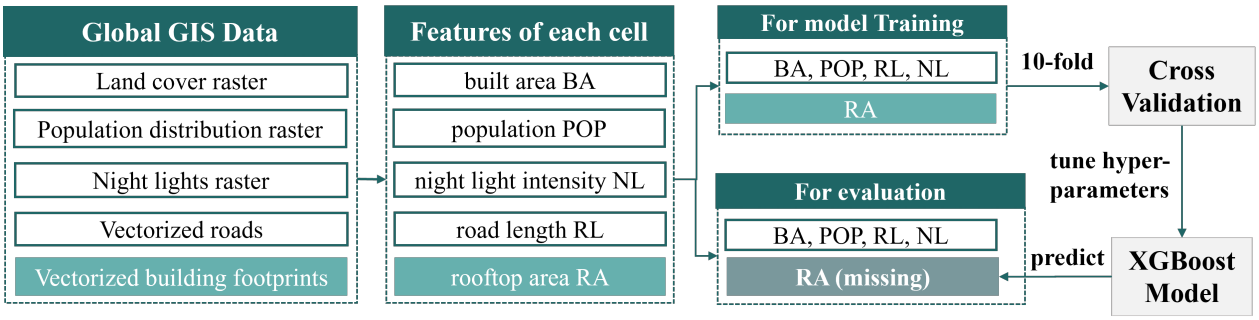

Figure S12: Framework for rooftop area assessment using XGBoost regression model.

In this framework, we initially divide the global landmass into fishnet cells with a spatial resolution of 0.125°×0.125°, ensuring that each ERA5 grid cell (0.25°×0.25°) encompasses four corresponding fishnet cells. Subsequently, we collect publicly accessible datasets, including global land cover raster data (with a resolution of 10 m) from the Environmental Systems Research Institute (ESRI) [38], population distribution raster data (with a resolution of 100 m) from WorldPop [39], VIIRS global night lights raster data (with a resolution of 500 m) [40], and vectorized road network and building footprints data from Microsoft AI [41]. For cells in China specifically, vectorized roads and rooftops data are from Open Street Map (OSM) [42] and another dataset containing rooftop information for 90 cities in China [35] due to the absence in the Microsoft AI dataset. Based on the fishnet cells and datasets, we use ArcGIS to calculate the built-up area (BA), population (POP), and average night light (NL) within each fishnet cell. Additionally, we determine the road length (RL) by measuring the total length of vectorized roads and assess the rooftop area (RA) by calculating the total area of building footprints within each fishnet cell's built-up area. Figure S13 shows the selected portions of built-up areas, roads, and building footprints within Bologna, Italy's fishnet cells. The yellow regions with gray borders represent blocks comprising built areas, while red regions and brown lines denote actual buildings and roads.

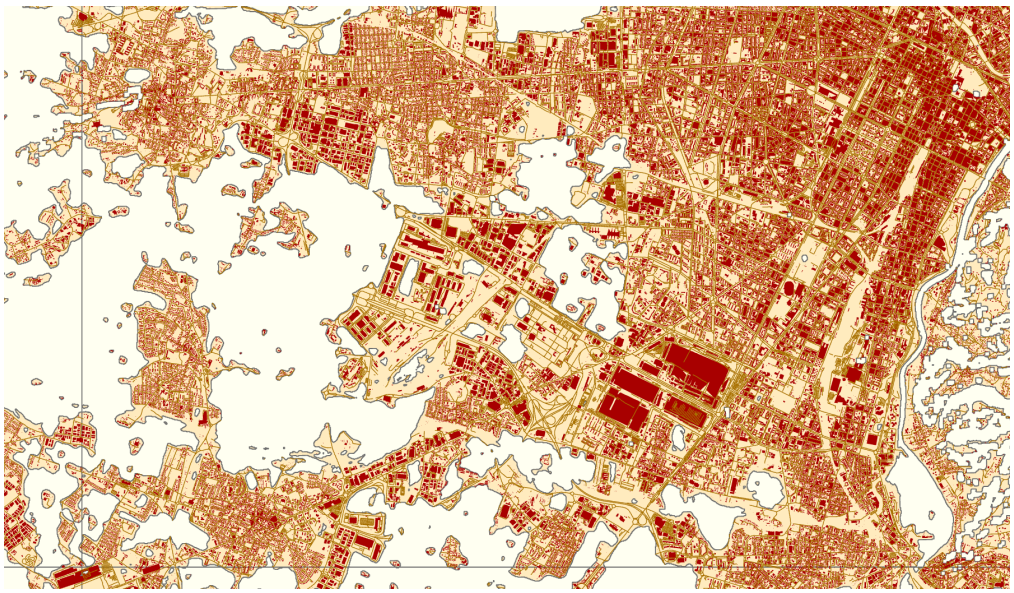

Figure S13: Illustration of Roof Vector Data Area.

We then divide the processed dataset into training and prediction sets based on the rooftop data. For those fishnet cells with vectorized rooftop data and also located within the built-up area, we use these cells as training and validation data. The remaining fishnet cells are divided into the prediction set and will be predicted by the trained regression model. Before training the regression model, we first examine the correlation coefficient between rooftop area and road length, built-up area, population and night lights, and the results are consistent with previous studies [36, 37]. We show the correlation coefficients in Figure S14.

The machine learning (ML) model, based on the XGBoost algorithm, utilizes BA, POP, RL, and NL as independent variables and RA as the dependent variable. It is then trained and tested using data from fishnet cells that have positive BA and RA values. Before model training, missing values of POP, RL, and NL are interpolated through iterative multiple regression imputation. After tuning hyperparameters via 10-fold cross-validation, the ML model achieves an accuracy score (R^2 value) of 0.865 on the test data. The rooftop area (RA) for both the training set cells and all evaluated fishnet cells is shown in Figure S15.

Finally, we adopt the appropriate area for developing distributed solar PV power in each fishnet cell as 0.40, 0.35 [37], and 0.30 in the open, base, and conservative scenarios, respectively. The suitable area within each ERA5 land grid cell was obtained by aggregating the corresponding fishnet cells and is illustrated in Figure S16.

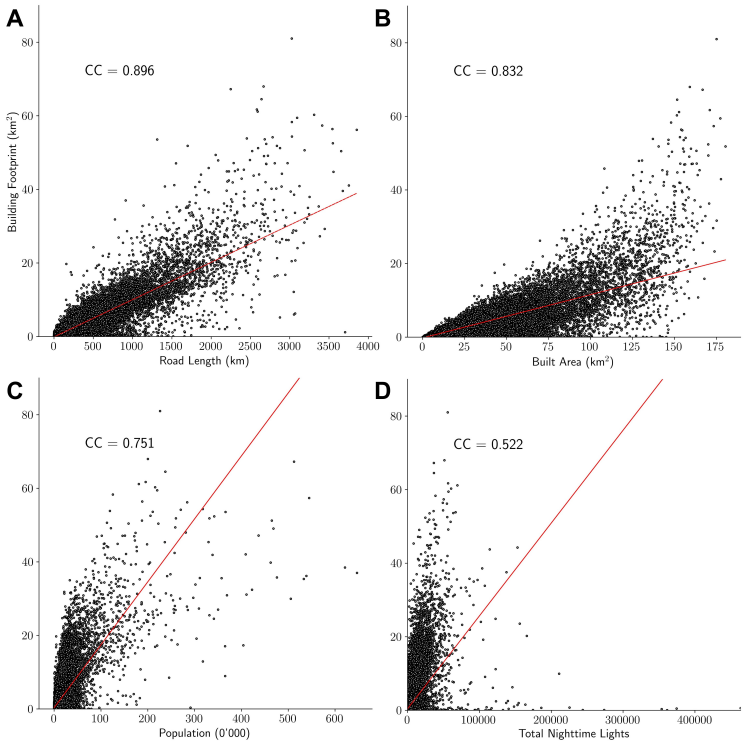

Figure S14: Correlation coefficient between rooftop area and road length (A), built-up area (B), population (C), and night lights (D).

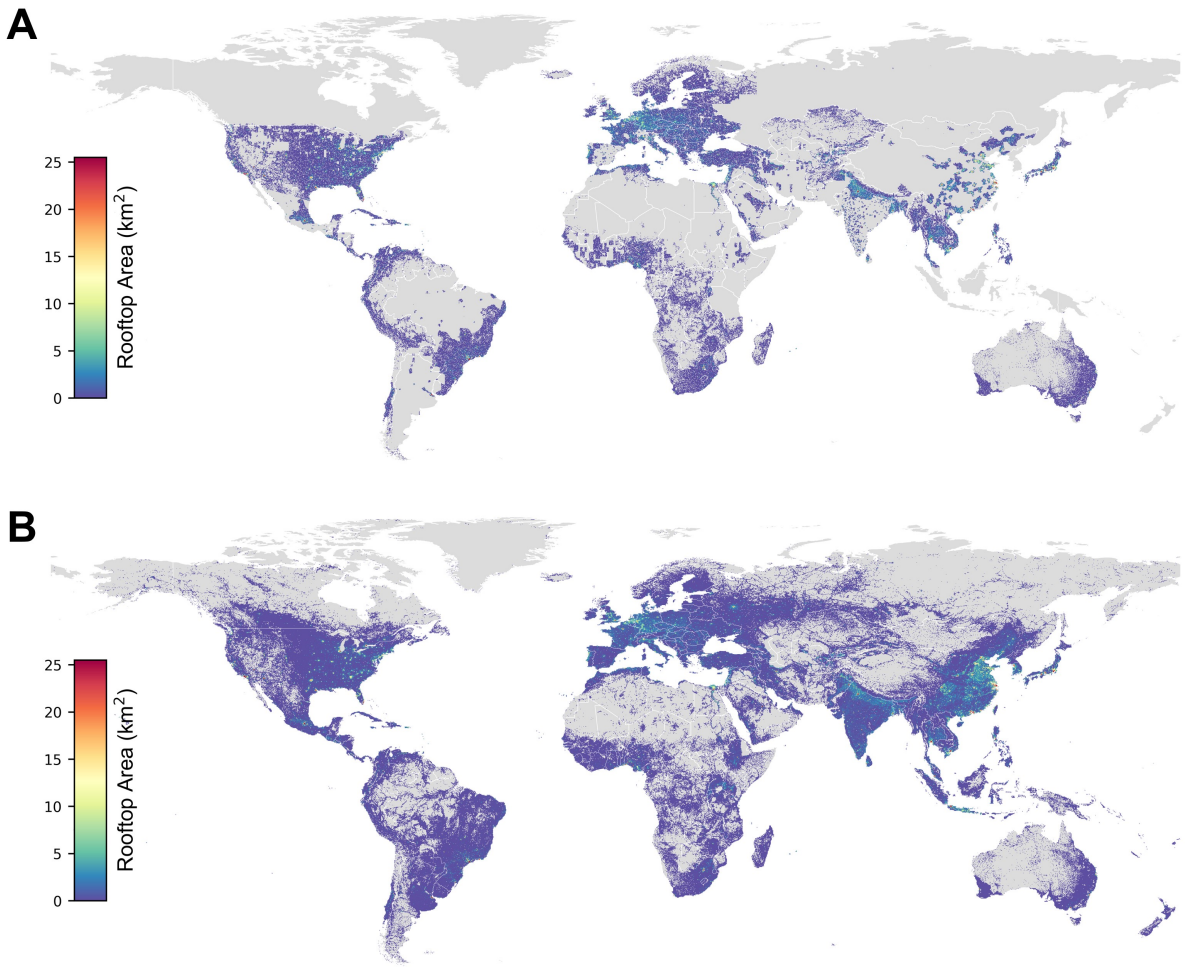

Figure S15: Rooftop area (km^2) of training data (A) fed into XGBoost model, and predicted results (B) by the trained XGBoost model.

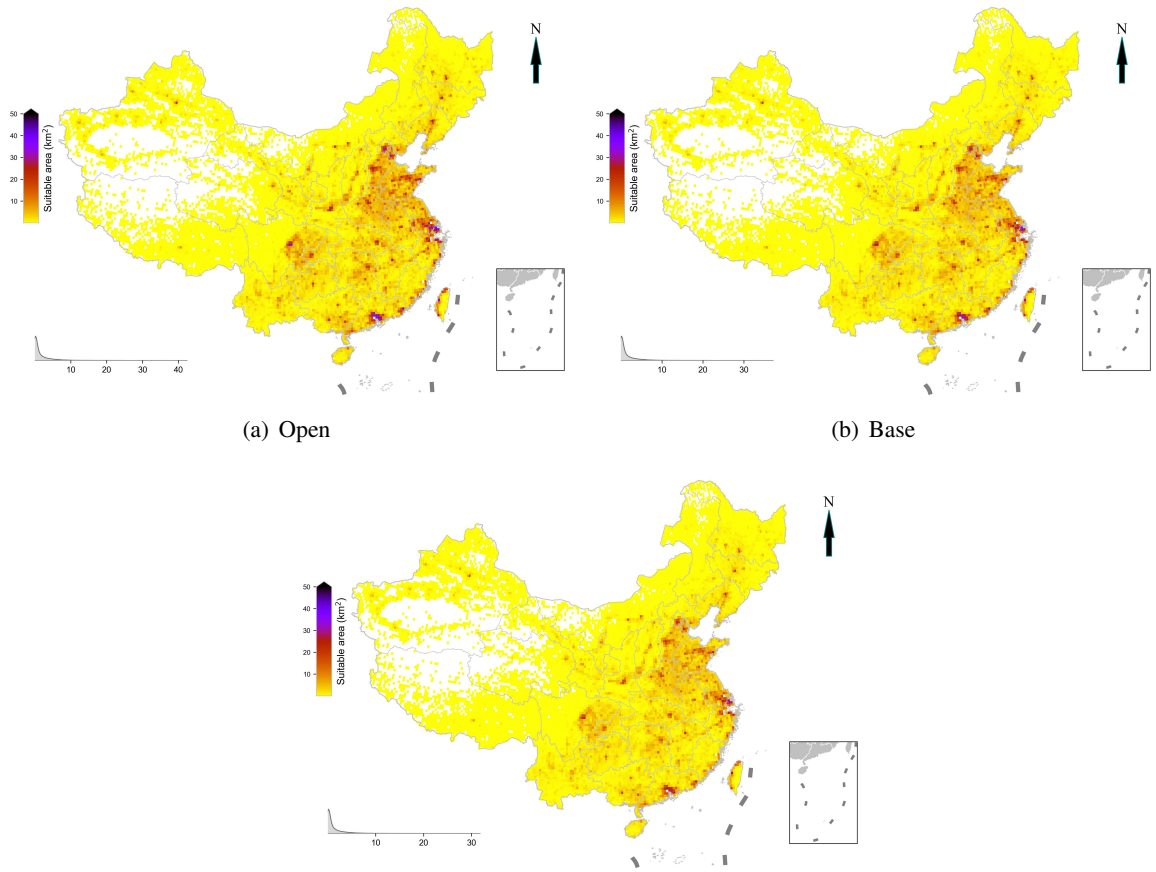

(a) Open

(b) Base

(c) Conservative

Figure S16: Suitable area (km^2) for building distributed solar PV in each grid cell in open (a), base (b), and conservative (c) scenario.

2.6 Assessment of installation capacity potential

The installation capacity potential for wind, solar PV, and CSP can be obtained by multiplying the suitable installation area (km^2) and the installation density (MW/km^2), as follows:

$$Cap_g^{max} = SA \times \mathcal{D}_g, \tag{S2-16}$$

where Cap_g^{max} is the installation capacity potential (MW) of power g (wind, solar PV, or CSP), SA is the suitable installation area (km^2) in each grid cell, and $\mathcal{D}_g$ is the installation density (MW/km^2) of power g.

Wind power The spacing between wind turbines is a key factor in wind farm design, as it impacts both power production and turbine structural loading. The optimal spacing is primarily determined by the predominant wind direction and turbine rotor diameter, with previous studies suggesting a spacing of 5–10 rotor diameters between turbines to mitigate wake effects and turbine fatigue [6, 43]. In this study, focusing on utility-scale turbines with above 1 MW nameplate capacity, we calculate the installation densities using NREL turbine specifications [1] and the adopted 7×7 rotor diameters spacing [6, 44]. The resulting onshore wind power installation densities range from 2.40 to 5.50 MW/km^2, while offshore densities range from

4.80 to 6.30 MW/km^2, as detailed in Tables S6 and S7. For evaluating wind power potentials, we use reference installation densities of 4.0 MW/km^2 for onshore wind [6] and 5.0 MW/km^2 for offshore wind [44], as defined in Equation S2-16. We show the resulting installation capacity potential (MW) for onshore and offshore wind in open, base, and conservative scenarios for each cell and province in Figure S17 and Table S8–S9, respectively. Additionally, the annual power generation potential can be calculated by the installation capacity potential and the annual average capacity factor.

Table S6: Onshore wind turbine parameters.

Wind turbine model	Rotor diameter (m)	Nameplate capacity (MW)	Installation density (MW/km^2)
2020 ATB NREL Reference 5.5 MW	175.0	5.50	3.60
2020 ATB NREL Reference 7 MW	200.0	7.00	3.50
BAR BAU LowSP 3.25 MW	166.0	3.25	2.40
BAR BAUa 5 MW	167.4	5.00	3.60
BAR LBNL-IEA 3.3 MW	156.0	3.30	2.72
BAR HighSP 5 MW	135.0	5.00	5.50
BAR LowSP 4.5 MW	194.0	4.50	2.40
BAR LowSP 6.5 MW	234.0	6.50	2.40
DOE GE 1.5 MW	77.0	1.50	5.00
IEA 3.4 MW Reference	130.0	3.37	4.00

Table S7: Offshore wind turbine parameters.

Wind turbine model	Rotor diameter (m)	Nameplate capacity (MW)	Installation density (MW/km^2)
2016CACost NREL Reference 6 MW 155	155.0	6.00	5.00
2016CACost NREL Reference 8 MW 180	180.0	8.00	5.00
2016CACost NREL Reference 10 MW 205	205.0	10.00	4.80
2019ORCost NREL Reference 12 MW 222	222.0	12.00	4.90
2019ORCost NREL Reference 15 MW 248	248.0	15.00	4.90
2020ATB NREL Reference 12 MW 214	214.0	12.00	5.20
2020ATB NREL Reference 15 MW 240	240.0	15.00	5.20
2020ATB NREL Reference 18 MW 263	263.0	18.00	5.20
DTU 10 MW 178 RWT v1	178.0	10.00	6.30
IEA 10 MW 198 RWT	198.0	10.00	5.10
IEA 15 MW 240 RWT	240.0	15.00	5.20
LEANWIND 8 MW 164 RWT	164.0	8.00	6.00
NREL 5 MW 126 RWT	126.0	5.00	6.25

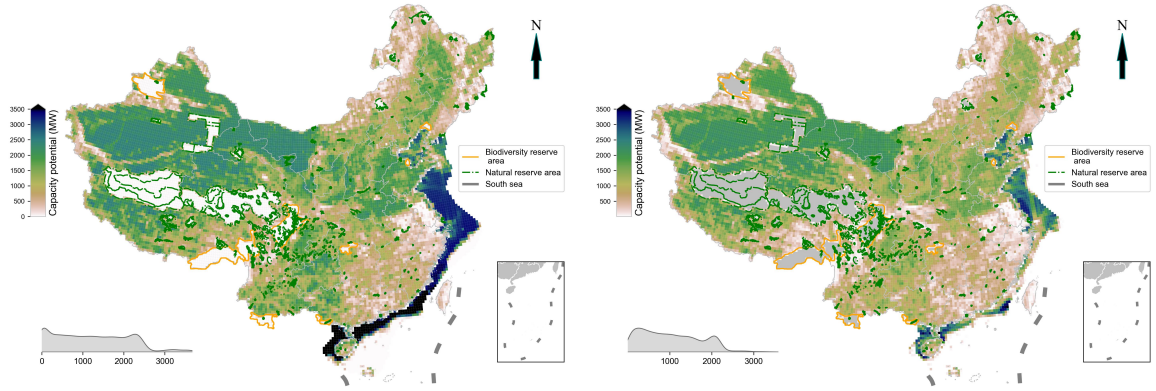

(a) Open (b) Base

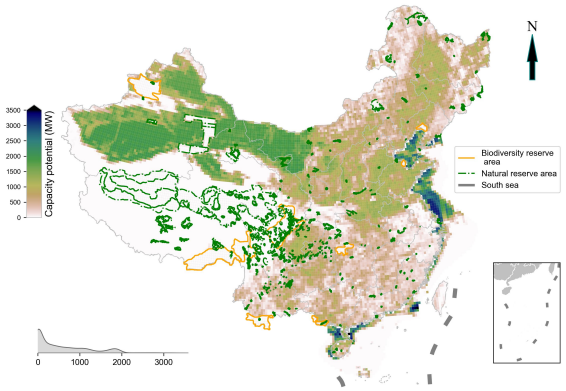

(c) Conservative

Figure S17: Installation capacity potential (MW) for onshore and offshore wind power in each grid cell in open (a), base (b) and, conservative (c) scenarios.

Table S8: Provincial installation capacity potential (GW) of onshore wind in mainland China.

Province	Conservative	Base	Open	Province	Conservative	Base	Open
Anhui	96	135	174	Jilin	205	266	327
Beijing	14	21	27	Liaoning	148	199	248
Chongqing	58	103	148	Mengdong	371	481	589
Fujian	46	88	123	Mengxi	1,201	1,427	1,651
Gansu	650	920	1,124	Ningxia	75	100	123
Guangdong	85	124	158	Qinghai	269	975	1,206
Guangxi	137	244	353	Shaanxi	184	285	392
Guizhou	142	277	395	Shandong	245	329	411
Hainan	32	43	54	Shanghai	1	2	2
Hebei	244	342	434	Shanxi	225	326	416
Heilongjiang	480	619	757	Sichuan	165	343	507
Henan	233	321	407	Tianjin	13	17	21
Hubei	126	208	291	Xinjiang	2,783	3,823	4,528
Hunan	106	166	223	Xizang	0	1,135	1,617
Jiangsu	56	75	93	Yunnan	158	370	594
Jiangxi	88	130	168	Zhejiang	18	31	45
				Total	8,654	13,925	17,606

Table S9: Provincial installation capacity potential (GW) of offshore wind in mainland China.

Province	Conservative	Base	Open	Province	Conservative	Base	Open
Fujian	61	89	257	Liaoning	106	144	147
Guangdong	141	266	579	Shandong	162	211	321
Guangxi	23	26	42	Shanghai	22	68	115
Hainan	31	49	105	Tianjin	8	8	8
Hebei	68	69	69	Zhejiang	62	151	505
Jiangsu	311	382	530	Total	995	1,463	2,678

Solar power In this study, we assume a fixed tilt model for the installation of solar PV panels to assess the capacity potential of utility-scale and distributed solar PV power. Under this assumption, it becomes imperative to calculate the optimal tilt, orientation, and inter-panel distance in each grid cell. Initially, we determine the corresponding optimal tilt based on the latitude of each grid cell as below [16]:

$$\Sigma = 1.3793 + \theta \times [1.2011 + \theta \times (-0.0014404 + \theta \times 0.000080509)], \tag{S2-17}$$

where θ is the latitude of the grid cell. In assessing the solar PV resource potential in China (or the Northern Hemisphere), it is hypothesized that the PV arrays are oriented facing the equator to maximize solar radiation receipt. Inter-panel spacing can be determined by avoiding shading from adjacent panels. Given that shadows reach maximum length in the Northern Hemisphere on the winter solstice at 3 PM, the solar altitude and azimuth at this time are adopted to evaluate the inter-panel distance to preclude potential shading concerns. The equation for computing separation between adjoining PV panels is [9]:

$$D = L \times \left(\cos \Sigma + \frac{\sin \Sigma}{\tan \beta_n} \times \cos \phi_s \right), \tag{S2-18}$$

where D is the distance between adjacent PV panels, L is the length of the PV panel, Σ is the optimal tilt angle in radians, β_n and ϕ_s are the solar altitude angle and azimuth angle at 3 PM on the winter solstice in the Northern Hemisphere, respectively. After determining the distance D, we can calculate the packing factor, which represents the ratio of the area occupied by PV panels to the installation area, as follows:

$$PF = \frac{L}{D} = \frac{1}{\cos \Sigma + \frac{\sin \Sigma}{\tan \beta_n} \times \cos \phi_s}. \tag{S2-19}$$

Finally, we assume a unit capacity of 161.9 W/m^2 [16] and determine the installation density for solar power in each grid cell by multiplying it with the packing factor, denoted as $\mathcal{D}_{pv} = 161.9 \times PF$. The installation density is consistent for utility-scale and distributed solar PV within the same grid cell. We show the resulting installation capacity potential (MW) for utility-scale and distributed solar PV in each cell and provincial grid in Figure S18 and Table S10, respectively.

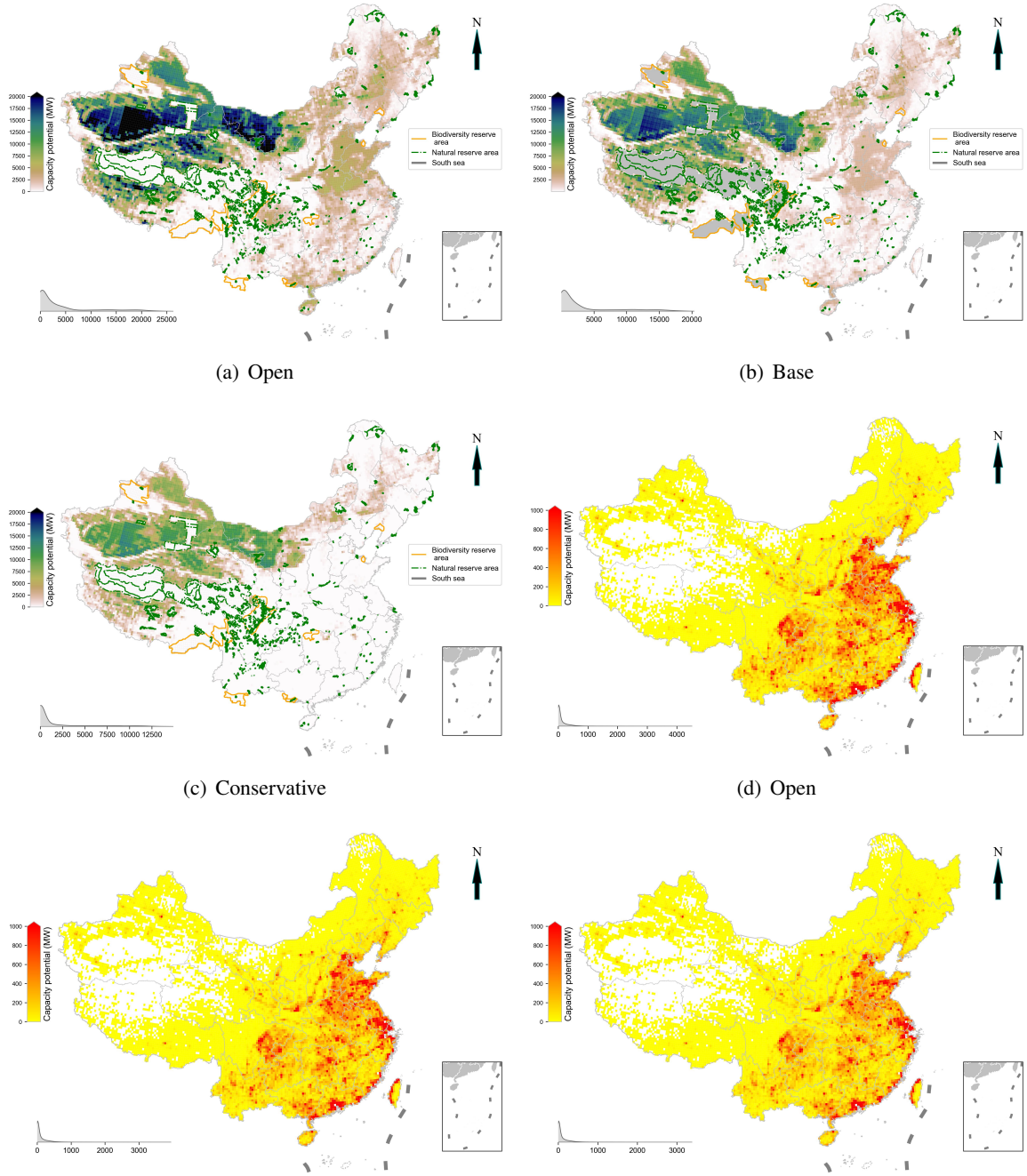

(a) Open (b) Base

(c) Conservative (d) Open

(e) Base (f) Conservative

Figure S18: Installation capacity potential (MW) for utility-scale (a, b, and c) and distributed solar PV (d, e, and f) in each grid cell in open, base, and conservative scenario.

Table S10: Provincial installation capacity potential (GW) of UPV and DPV in mainland China.

Province	Utility-scale solar PV			Distributed solar PV		
	Conservative	Base	Open	Conservative	Base	Open
Anhui	1	224	453	54	63	72
Beijing	0	24	51	12	14	16
Chongqing	0	39	111	25	30	34
Fujian	1	36	94	36	42	48
Gansu	2,583	3,878	5,159	23	26	30
Guangdong	2	189	417	107	125	143
Guangxi	1	182	433	55	64	74
Guizhou	1	29	119	42	49	56
Hainan	2	78	161	9	11	12
Hebei	26	373	754	66	77	88
Heilongjiang	405	884	1,385	16	18	21
Henan	1	442	919	80	93	106
Hubei	9	187	400	52	61	69
Hunan	28	156	340	67	78	90
Jiangsu	2	189	377	79	92	105
Jiangxi	15	140	306	48	56	64
Jilin	178	426	695	14	17	19
Liaoning	18	196	414	29	33	38
Mengdong	421	798	1,231	9	11	12
Mengxi	5,238	7,736	10,180	12	14	16
Ningxia	113	218	339	7	8	9
Qinghai	2,825	4,519	6,241	5	6	7
Shaanxi	118	285	492	26	31	35
Shandong	12	477	967	100	117	134
Shanghai	2	18	35	17	19	22
Shanxi	14	172	411	27	32	37
Sichuan	53	234	524	84	98	112
Tianjin	6	35	64	10	12	14
Xinjiang	13,366	20,383	26,867	17	20	23
Xizang	1,843	3,370	5,208	4	4	5
Yunnan	1	57	182	56	65	74
Zhejiang	1	53	115	56	66	75
Total	27,286	46,027	65,444	1,244	1,452	1,660

For concentrating solar power, we use the packing factor of 0.37 [27] multiplying the maximum generation capacity of the per-area collector of 100 W/m^2 as the installation density, which is 37 MW/m^2. We show the cell-level installation capacity potential of CSP in Figure S19.

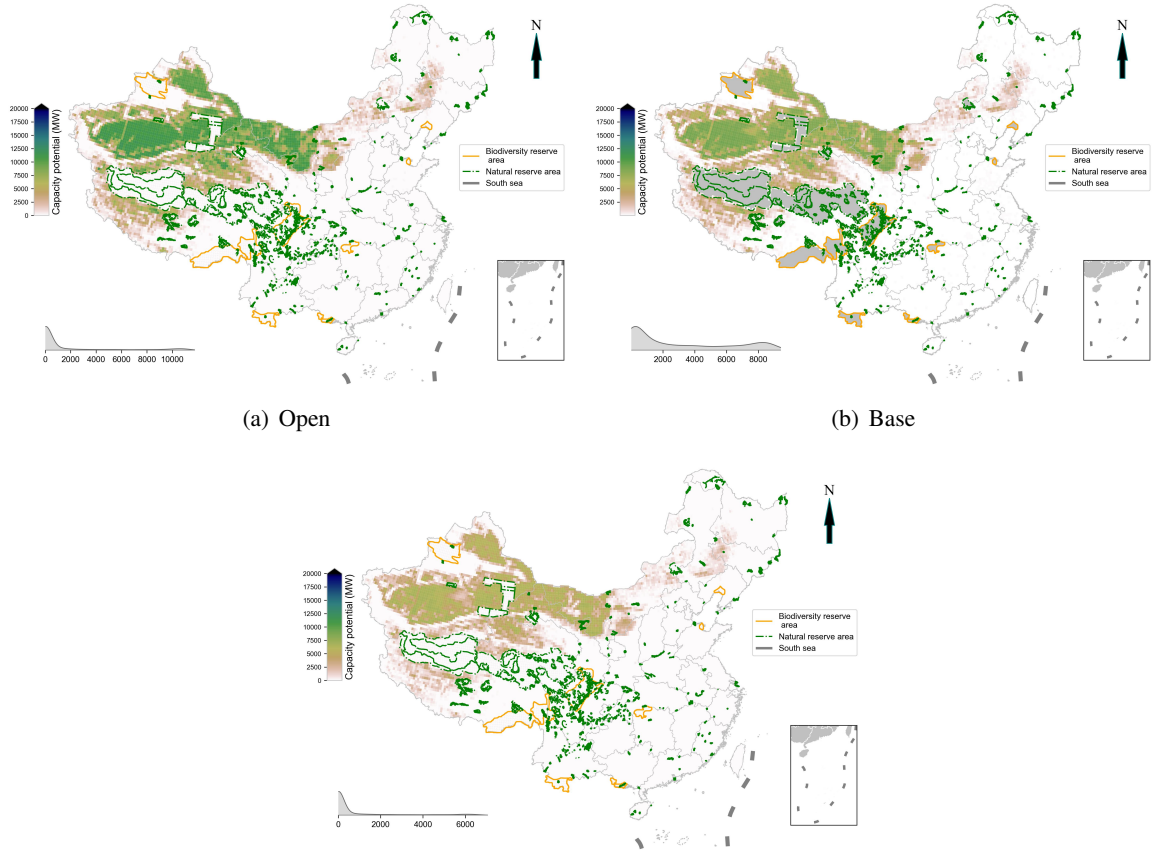

(a) Open (b) Base

(c) Conservative

Figure S19: Installation capacity potential (MW) for concentrating solar power in each grid cell in open (a), base (b), and conservative (c) scenarios.

References

[1] National Renewable Energy Laboratory. 2020 annual technology baseline: Nrel reference 7mw. https://nrel.github.io/turbine-models/2020ATB_NREL_Reference_7MW_200.html, 2020.

[2] Parthiv Kurup and Craig S Turchi. Parabolic trough collector cost update for the system advisor model (sam). Technical report, National Renewable Energy Lab.(NREL), Golden, CO (United States), 2015.

[3] Hans Hersbach, Bill Bell, Paul Berrisford, Shoji Hirahara, András Horányi, Joaquín Muñoz-Sabater, Julien Nicolas, Carole Peubey, Raluca Radu, Dinand Schepers, Adrian Simmons, Cornel Soci, Saleh Abdalla, Xavier Abellan, Gianpaolo Balsamo, Peter Bechtold, Gionata Biavati, Jean Bidlot, Massimo Bonavita, Giovanna Chiara, Per Dahlgren, Dick Dee, Michail Diamantakis, Rossana Dragani, Johannes Flemming, Richard Forbes, Manuel Fuentes, Alan Geer, Leo Haimberger, Sean Healy, Robin J. Hogan, Elías Hólm, Marta Janisková, Sarah Keeley, Patrick Laloyaux, Philippe Lopez, Cristina Lupu, Gabor Radnoti, Patricia Rosnay, Iryna Rozum, Freja Vamborg, Sebastien Villaume, and Jean-Noël Thépaut. The ERA5 global reanalysis. *Quarterly Journal of the Royal Meteorological Society*, 146(730):1999–2049, 2020.

[4] Patrick R. Brown and Audun Botterud. The Value of Inter-Regional Coordination and Transmission in Decarbonizing the US Electricity System. *Joule*, 5(1):115–134, January 2021.

[5] Oleg A. Alduchov and Robert E. Eskridge. Improved Magnus Form Approximation of Saturation Vapor Pressure. *Journal of Applied Meteorology and Climatology*, 35(4):601–609, April 1996.

[6] Tianguang Lu, Peter Sherman, Xinyu Chen, Shi Chen, Xi Lu, and Michael McElroy. India's potential for integrating solar and on- and offshore wind power into its energy system. *Nature Communications*, 11(1):4750, 2020.

[7] Qiang Wang, Kun Luo, Renyu Yuan, Sanxia Zhang, and Jianren Fan. Wake and performance interference between adjacent wind farms: Case study of xinjiang in china by means of mesoscale simulations. *Energy*, 166:1168–1180, 2019.

[8] Marine Regions. The intersect of the Exclusive Economic Zones and IHO areas, 2023. https://www.marineregions.org/sources.php#ihoeez.

[9] Shi Chen, Xi Lu, Yufei Miao, Yu Deng, Chris P. Nielsen, Noah Elbot, Yuanchen Wang, Kathryn G. Logan, Michael B. McElroy, and Jiming Hao. The Potential of Photovoltaics to Power the Belt and Road Initiative. *Joule*, 3(8):1895–1912, August 2019.

[10] Patrick R Brown and Francis M O'Sullivan. Spatial and temporal variation in the value of solar power across united states electricity markets. *Renewable and Sustainable Energy Reviews*, 121:109594, 2020.

[11] A. P. Dobos. PVWatts Version 5 Manual. Technical Report NREL/TP-6A20-62641, National Renewable Energy Lab. (NREL), Golden, CO (United States), 2014.

[12] Sonia Jerez, Isabelle Tobin, Robert Vautard, Juan Pedro Montávez, Jose María López-Romero, Françoise Thais, Blanka Bartok, Ole Bøssing Christensen, Augustin Colette, Michel Déqué, Grigory Nikulin, Sven Kotlarski, Erik van Meijgaard, Claas Teichmann, and Martin Wild. The impact of climate change on photovoltaic power generation in Europe. *Nature Communications*, 6(1):10014, December 2015. Number: 1 Publisher: Nature Publishing Group.

[13] Yadong Lei, Zhili Wang, Deying Wang, Xiaoye Zhang, Huizheng Che, Xu Yue, Chenguang Tian, Junting Zhong, Lifeng Guo, Lei Li, et al. Co-benefits of carbon neutrality in enhancing and stabilizing solar and wind energy. *Nature Climate Change*, pages 1–8, 2023.

[14] David E. H. J. Gernaat, Harmen Sytze de Boer, Vassilis Daioglou, Seleshi G. Yalew, Christoph Müller, and Detlef P. van Vuuren. Climate change impacts on renewable energy supply. *Nature Climate Change*, 11(2):119–125, February 2021. Number: 2 Publisher: Nature Publishing Group.

[15] Julia A Crook, Laura A Jones, Piers M Forster, and Rolf Crook. Climate change impacts on future photovoltaic and concentrated solar power energy output. *Energy & Environmental Science*, 4(9):3101–3109, 2011.

[16] Shi Chen, Xi Lu, Yufei Miao, Yu Deng, Chris P. Nielsen, Noah Elbot, Yuanchen Wang, Kathryn G. Logan, Michael B. McElroy, and Jiming Hao. The potential of photovoltaics to power the belt and road initiative. *Joule*, 3:1895–1912, 8 2019.

[17] Xi Lu, Michael B McElroy, Chris P Nielsen, Xinyu Chen, and Junling Huang. Optimal integration of offshore wind power for a steadier, environmentally friendlier, supply of electricity in china. *Energy Policy*, 62:131–138, 2013.

[18] Xinliang Xu, Jiyuan Liu, Shuwen Zhang, Rendong Li, Changzhen Yan, and Shixin Wu. China Multi-Temporal Land Use/Cover Dataset (CNLUCC) (in Chinese). Resource and Environmental Science Data Center, 2018. `https://www.resdc.cn/DOI/DOI.aspx?DOIID=54`.

[19] State Forestry Administration (SFA) of the People's Republic of China. Notice on issues related to the use of forest land in the construction of photovoltaic power stations (in Chinese), 12 2015. `https://www.forestry.gov.cn/main/5925/20200414/090421953922884.html`.

[20] State Forestry and Grassland Administration (SFGA) of the People's Republic of China. Notice on regulating the use of forest land in the construction of wind farm projects. [EB/OL], 02 2019. `http://www.gov.cn/zhengce/zhengceku/2019-09/30/content_5435366.htm`.

[21] OpenTopography - Copernicus GLO-30 Digital Elevation Model, 2023. https://portal.opentopography.org/raster?opentopoID=OTSDEM.032021.4326.1.

[22] D. Yamazaki. MERIT DEM: A new high accuracy global digital elevation model, 2023. http://hydro.iis.u-tokyo.ac.jp/~yamadai/MERIT_DEM/index.html.

[23] General Bathymetric Chart of the Oceans (GEBCO). Gebco gridded bathymetry data, 2023. https://www.gebco.net/data_and_products/gridded_bathymetry_data/.

[24] World Bank. Global Shipping Traffic Density, 2023. https://datacatalog.worldbank.org/search/dataset/0037580/Global%20Shipping%20Traffic%20Density?version=4.

[25] Matthieu Le Tixerant, Damien Le Guyader, Françoise Gourmelon, and Betty Queffelec. How can automatic identification system (ais) data be used for maritime spatial planning? *Ocean & Coastal Management*, 166:18–30, 2018.

[26] Diego Silva Herran, Hancheng Dai, Shinichiro Fujimori, and Toshihiko Masui. Global assessment of onshore wind power resources considering the distance to urban areas. *Energy Policy*, 91:75–86, 2016.

[27] David EHJ Gernaat, Harmen Sytze de Boer, Vassilis Daioglou, Seleshi G Yalew, Christoph Müller, and Detlef P van Vuuren. Climate change impacts on renewable energy supply. *Nature Climate Change*, 11(2):119–125, 2021.

[28] Da Zhang, Ziheng Zhu, Shi Chen, Chongyu Zhang, Xi Lu, Xiliang Zhang, Xiaoye Zhang, and Michael R Davidson. Spatially resolved land and grid model of carbon neutrality in china. *Proceedings of the National Academy of Sciences*, 121(10):e2306517121, 2023.

[29] Ministry of Natural Resources of the People's Republic of China. Guidelines for industrial land use policy (2019 version) (in Chinese). [EB/OL], 04 2019. http://www.gov.cn/zhengce/zhengceku/2019-10/14/content_5439551.htm.

[30] Ministry of Land and Resources (MLR) of the People's Republic of China. Notice on supporting the development of photovoltaic power generation industry to regulate land management related work (in Chinese). [EB/OL], 2023. https://www.gov.cn/zhengce/zhengceku/2023-04/03/content_5749824.htm.

[31] Fuying Chen, Qing Yang, Niting Zheng, Yuxuan Wang, Junling Huang, Lu Xing, Jianlan Li, Shuanglei Feng, Guoqian Chen, and Jan Kleissl. Assessment of concentrated solar power generation potential in china based on geographic information system (gis). *Applied Energy*, 315:119045, 2022.

[32] The National People's Congress of the People's Republic of China. Land Administration Law of the People's Republic of China. [EB/OL], 9 2019. http://www.npc.gov.cn/npc/c30834/201909/d1e6c1a1eec345eba23796c6e8473347.shtml.

[33] Grassland Law of the People's Republic of China (in Chinese). [EB/OL], 4 2021. https://flk.npc.gov.cn/detail2.html?ZmY4MDgxODE3YWIyMmI4YTAxN2FiZDVhZDI4NjA1N2E.

[34] Guiding Opinions of the Ministry of Water Resources on Strengthening the control of shoreline space of river and lake waters (in Chinese). [EB/OL], 5 2022. https://www.gov.cn/gongbao/content/2022/content_5701574.htm.

[35] Zhixin Zhang, Zhen Qian, Teng Zhong, Min Chen, Kai Zhang, Yue Yang, Rui Zhu, Fan Zhang, Haoran Zhang, Fangzhuo Zhou, Jianing Yu, Bingyue Zhang, Guonian Lü, and Jinyue Yan. Vectorized rooftop area data for 90 cities in China. *Scientific Data*, 9(1):66, March 2022.

[36] Siddharth Joshi, Shivika Mittal, Paul Holloway, Priyadarshi Ramprasad Shukla, Brian Ó Gallachóir, and James Glynn. High resolution global spatiotemporal assessment of rooftop solar photovoltaics potential for renewable electricity generation. *Nature Communications*, 12(1):5738, October 2021.

[37] Zhixin Zhang, Min Chen, Teng Zhong, Rui Zhu, Zhen Qian, Fan Zhang, Yue Yang, Kai Zhang, Paolo Santi, Kaicun Wang, Yingxia Pu, Lixin Tian, Guonian Lü, and Jinyue Yan. Carbon mitigation potential afforded by rooftop photovoltaic in China. *Nature Communications*, 14(1):2347, April 2023.

[38] Krishna Karra, Caitlin Kontgis, Zoe Statman-Weil, Joseph C. Mazzariello, Mark Mathis, and Steven P. Brumby. Global land use / land cover with Sentinel 2 and deep learning. In *2021 IEEE International Geoscience and Remote Sensing Symposium IGARSS*, pages 4704–4707, July 2021.

[39] Forrest R. Stevens, Andrea E. Gaughan, Catherine Linard, and Andrew J. Tatem. Disaggregating census data for population mapping using random forests with remotely-sensed and ancillary data. *PloS One*, 10(2):e0107042, 2015.

[40] Christopher D. Elvidge. Annual Time Series of Global VIIRS Nighttime Lights Derived from Monthly Averages: 2012 to 2019. *Remote Sensing.*, 2021.

[41] Microsoft. Global Building ML Footprints. https://github.com/microsoft/GlobalMLBuildingFootprints, 2023.

[42] OpenStreetMapContributors. Openstreetmap data. https://www.openstreetmap.org, 2022.

[43] Xinyu Chen, Yaxing Liu, Qin Wang, Jiajun Lv, Jinyu Wen, Xia Chen, Chongqing Kang, Shijie Cheng, and Michael B. McElroy. Pathway toward carbon-neutral electrical systems in China by mid-century with negative CO2 abatement costs informed by high-resolution modeling. *Joule*, 5(10):2715–2741, 2021.

[44] Xinyang Guo, Xinyu Chen, Xia Chen, Peter Sherman, Jinyu Wen, and Michael McElroy. Grid integration feasibility and investment planning of offshore wind power under carbon-neutral transition in China. *Nature Communications*, 14(1):2447, 2023.